Model-Based Dynamic Control of Two-Degree-of-Freedom Modulation for Dual Active Half-Bridge Converter

Gun-Su Kim, *Student Member, IEEE*, Su-Bin Kang, *Student Member, IEEE*, Hyeon-Sik Kim, *Member, IEEE*, and Jehyuk Won, *Member, IEEE*

***Abstract*—This article proposes a model-based dynamic control for dual active half-bridge converters to satisfy both a loss-minimizing operation and a high-dynamic response. First, the loss-minimizing operation is analyzed based on a two-degree-of-freedom (2-DOF) modulation scheme, where control variables consist of a phase shift and a duty ratio. The modulation scheme is optimized to minimize the transformer root-mean-square current or to achieve a zero-voltage-switching condition under varying conditions. Moreover, the output voltage control should be designed to provide fast dynamic performance under source and load variations. Therefore, the voltage controller is unified with the modulation schemes, where a model-based control is adopted to improve the dynamics of 2-DOF modulation. A model-based calculation part reduces the burden of an error compensation part with a load current feedforward. Finally, the effectiveness of the proposed method is verified by the experimental results.**

***Index Terms*—Dual active half-bridge converter (DAHB), minimum root-mean-square (RMS) current, model-based control, zero-voltage switching (ZVS).**

I. Introduction

A dual active bridge (DAB) dc–dc converter has been widely adopted in several applications owing to its advantages such as zero-voltage switching, bidirectional power flow capability, and convenience of cascading and paralleling [1], [2], [3]. The DAB converter with a half-bridge structure can reduce the number of power MOSFETs and their driving circuits by using split dc capacitors on both sides compared to that with a full-bridge structure. Moreover, the spilt dc capacitors eliminate the dc component of the transformer magnetizing current in the steady state without additional control techniques. Therefore, it is preferred in a low-power system (below 750 W) because the cost, volume, and weight of the converter can be minimized [4], [5], [6], [7].

In the dual active half-bridge (DAHB) converter, the phase can be shifted from $-90°$ to $+90°$ to change the power transfer between the primary and secondary sides. For the maximum power transfer, the duty ratio is fixed at 0.5 and the phase shift is controlled to regulate the output voltage. It has been called the single phase shift, which is equivalent to one-degree-of-freedom (1-DOF) modulation. The 1-DOF modulation is widely utilized due to its simplicity. Moreover, the zero-voltage-switching (ZVS) condition can be achieved when a voltage conversion ratio is unity. However, the soft-switching range is limited as the voltage conversion ratio deviates further from unity, especially under light-load conditions. The circulating current through the switches and the transformer cannot be minimized under 1-DOF modulation, resulting in a significant reactive power flow [8], [9].

To improve the system's efficiency under different operating conditions, not only the phase shift but also the duty ratio can be controlled. This is called the asymmetric duty control, also known as two-degree-of-freedom (2-DOF) modulation [5], [9], [10], [11], [12], [13]. The 2-DOF modulation can improve the system efficiency by minimizing the circulating current or extending the ZVS region in the light-load conditions for the DAHB converter. The closed-loop control was proposed to minimize the peak current flowing through the inductor, where the peak current can be easily calculated in real time [10]. Similarly, 2-DOF modulation has been presented to minimize the root-mean-square (RMS) current flowing through the inductor [11], [12]. These schemes are optimized to decrease conduction loss, where the RMS current of the circulating loop should be minimized. Furthermore, 2-DOF modulation has been utilized to satisfy the ZVS conditions under a nonunity voltage conversion ratio [5], [9], [13]. These schemes guarantee the ZVS of all switching devices despite the higher RMS current, which is adopted to minimize the switching loss.

A three-degree-of-freedom (3-DOF) modulation has also been proposed, where the duty ratios of the two half-bridges can

Received 20 October 2024; revised 11 January 2025; accepted 29 January 2025. Date of publication 4 February 2025; date of current version 20 March 2025. This work was supported in part by the Korea Institute of Energy Technology Evaluation and Planning and the Ministry of Trade, Industry & Energy of the Republic of Korea, under Grant 20214000000060, and in part by the Basic Science Research Program through the National Research Foundation of Korea funded by the Ministry of Education under Grant RS-2023-00237518. Recommended for publication by Associate Editor J. He. *(Corresponding author: Hyeon-Sik Kim.)*

Gun-Su Kim and Su-Bin Kang are with the Department of Next-Generation Smart Energy System Convergence, Gachon University, Seongnam 13120, South Korea (e-mail: soae97@gachon.ac.kr; for01099@gachon.ac.kr).

Hyeon-Sik Kim is with the Department of Electrical Engineering, Gachon University, Seongnam 13120, South Korea (e-mail: hyeonsik@gachon.ac.kr).

Jehyuk Won is with the Department of Electrical and Electronics Engineering, Kangwon National University, Chuncheon 24341, South Korea (e-mail: jhwon@kangwon.ac.kr).

Color versions of one or more figures in this article are available at https://doi.org/10.1109/TPEL.2025.3538613.

Digital Object Identifier 10.1109/TPEL.2025.3538613

TABLE I
COMPARISON OF THE PROPOSED METHOD WITH EXISTING METHODS

References	Control degrees of freedom	Number of sensors	Controller implementation	Minimum RMS operation with ZVS	Dynamic performance of output voltage
[4]	2	2	Two PI controllers	Limited	Slow
[5]	2	2	Two PI controllers with calculations	Satisfied	Slow
[6]	3	2	Three PI controllers with calculations	Satisfied	Slow
[7]	3	2	Three PI controllers	Limited	Slow
Proposed method	2	3	Model-based control with PI compensator	Satisfied	Fast

be controlled in different ways. These modulations can further minimize the converter loss by calculating the peak current [14] or the minimum RMS current solution [6], [15] for a given power at the light-load conditions. However, the 3-DOF modulation increases the complexity of the control, which requires offline calculations to simplify operation or the closed-loop control to adjust three control variables simultaneously. Thus, the 2-DOF modulation has advantages over the 3-DOF modulation in terms of computational complexity and control dynamics.

The transient responses to load current or input voltage variations should be discussed to improve the control dynamics. The 2-DOF or 3-DOF modulations are mostly implemented using multiple proportional-integral (PI) controllers with different bandwidths, where the duty ratio is controlled by an inner slow control loop after the phase shift is adjusted [5], [6], [11]. These control schemes are easy to implement and suppress interference between the control loops with different dynamics. However, the transient responses such as source and load changes would be degraded due to the slow control dynamics. Moreover, the duty ratio should be set to 0.5 to transfer the required power above a certain power level, which requires the 1-DOF modulation. However, the transitions between the 1-DOF and 2-DOF modulation schemes were not considered. The dynamics of the DAHB converter should be analyzed not only to increase the control bandwidth but also to provide a smooth transition. The features of the above algorithms on the DAHB converter can be summarized in Table I. From Table I, it is easy to observe that the proposed scheme can achieve the best dynamic performance among these five schemes, and the proposed scheme can also minimize the RMS current while achieving ZVS conditions or not.

Generally, the PI controller is adopted to regulate the output voltage where a load current feedforward (LCFF) could be added to improve the transient response [16]. However, it is difficult to achieve linear dynamic characteristics using this conventional method because of the nonlinear relationship between the phase shift and the power transfer. A look-up table (LUT) solution can be applied to overcome these constraints [17]. However, the LUT methods require an accurate interpolation algorithm to minimize an approximation error. Recently, a model-based control has been applied to the DAB converter to improve the control dynamics. It has been modeled based on the power transfer equation, where the effects of the input voltage, output voltage, and load current are fully considered [18], [19], [20]. Similarly, the model-based voltage controller can be designed with a feedforward loop for the DAHB converter. However, none of these schemes can simultaneously improve system efficiency and provide excellent dynamic control of DAHB converters. Therefore, the voltage controller should be integrated with the modulation schemes to enhance both efficiency and dynamic performance.

In this article, the 2-DOF modulation scheme is analyzed to minimize the transformer RMS current and to satisfy the ZVS conditions. A power transfer equation is derived as a function of the phase shift and duty ratio to improve the efficiency of the DAHB converter. These modulation schemes are unified with the model-based voltage controller, which consists of an error compensation part and a model-based calculation part. The model-based calculation derives 2-DOF modulation references, i.e., the phase shift and the duty ratio, where the minimum current operation is solved by analytical methods in real time. Furthermore, the error compensation is implemented by the PI controller with LCFF, where the PI controller minimizes the steady-state error and the LCFF improves the control dynamics. The proposed controller improves both the system efficiency under steady-state conditions and the dynamic response under transient conditions, especially in the input voltage fluctuation and load disturbance conditions. The validity of the proposed controller is verified by experimental results.

The contents of this research, previously presented in [21], have been largely revised for better understanding. The proposed method can minimize not only the conduction loss but also the switching loss where ZVS criteria are considered. The gain setting process and loss distributions are discussed to achieve faster dynamics and higher efficiency of the DAHB converter under varying constraints. Moreover, extensive experimental results are included to clarify the effectiveness of the proposed scheme.

II. OPERATING PRINCIPLE OF DAHB CONVERTER

Fig. 1 shows a circuit schematic of the DAHB converter. The input voltage dc port V_{in} is interfaced with the output voltage dc port V_{out}, where S_1 and S_2 are the primary-side half-bridges and S_3 and S_4 are the secondary-side half-bridges. The primary- and secondary-side transformer voltages are represented by v_{ab} and v_{cd}, respectively, which are referred to as input ports. In this article, the magnetizing inductance is assumed to be greater than the leakage inductance, i.e., $L_m >> L_{lk}$, where the magnetizing current can be neglected [22]. L_{lk} denotes the primary-referred

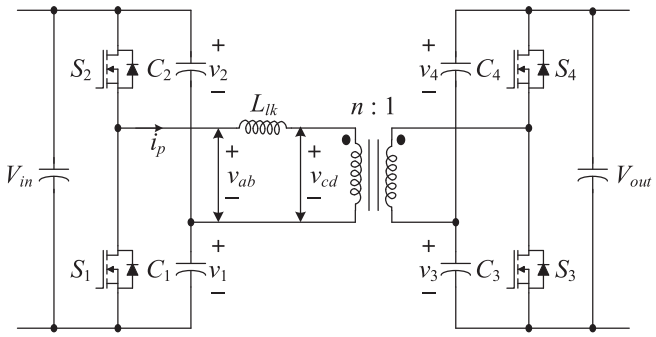

Fig. 1. Topology of the dual active half-bridge converter.

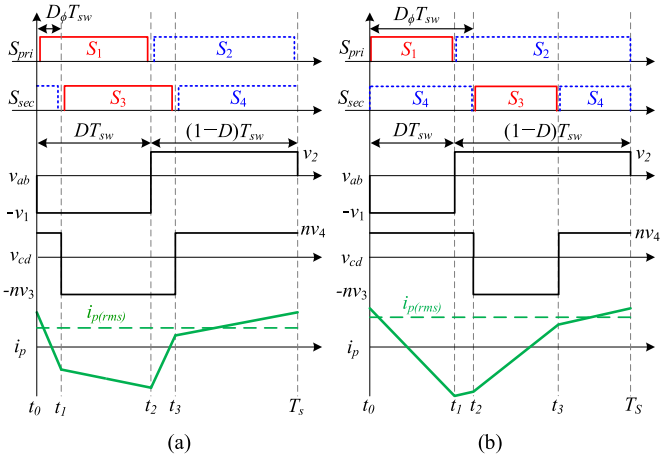

Fig. 2. Typical operating waveforms of 2-DOF modulation. (a) Case A: $0 \le D_\phi \le D$. (b) Case B: $D \le D_\phi$.

TABLE II
AVERAGE HALF-BRIDGE CAPACITOR VOLTAGE

Voltage	Expression	Voltage	Expression
v_1	DV_{in}	v_3	DV_{out}
v_2	$(1\text{-}D)V_{in}$	v_4	$(1\text{-}D)V_{out}$

leakage inductance of the transformer, and n represents the turn ratio.

Fig. 2 shows the typical operating waveforms of gate signals, transformer voltages, and currents, where 2-DOF modulation is applied. The duty ratio for the low-side switches is defined as D and the phase shift is defined as $D_\phi T_{sw}$, where T_{sw} is the switching time, i.e., $1/f_{sw}$. In this case, the split dc capacitors C_1–C_4, are large enough to keep the dc voltages approximately constant over a switching cycle. The split dc capacitor voltages from v_1 to v_4 are determined by the flux-second balance of the leakage inductance of the transformer L_{lk}. The results are summarized in Table II, where the duty ratio can result in different split voltages. The primary-side current of transformer i_p is approximated as a piecewise linear function according to the switching patterns.

The power flow is symmetrical about $D = 0.5$ for the same D_ϕ due to the symmetric structure of the DAHB converter. The DAHB converter can achieve maximum efficiency at a duty ratio of 0.5 or less [12]. Thus, this article is focused on analyzing two cases as shown in Fig. 2(a) and (b) for the forward operation, i.e., $D_\phi \ge 0$. Fig. 2(a) shows the waveforms in case A $(0 \le D_\phi \le D)$ for minimizing the transformer RMS current, i.e., $I_{p(rms)}$, which can reduce the conduction loss. Fig. 2(b) shows the waveforms in case B $(D \le D_\phi)$ for achieving the ZVS condition of S_3 turn-ON, i.e., $i_p(t_2) < 0$, which minimizes the switching loss. Likewise, the operating waveform can be analyzed in the two cases as $0 \le |D_\phi| \le D$ or $D \le |D_\phi|$ for the reverse operation, where $D_\phi < 0$. The instantaneous currents in case A from t_0 to t_3, i.e., from $i_p(t_0)$ to $i_p(t_3)$, can be derived by the steady-state assumption, as follows:

$$\begin{aligned}
i_p(t_0) &= \frac{-T_{sw}}{2L_{lk}}[V_{in}(-D+D^2)+nV_{out}(D-2DD_\phi-D^2)]\\
i_p(t_1) &= \frac{T_{sw}}{2L_{lk}}[V_{in}(-2D_\phi+2DD_\phi+D-D^2)+nV_{out}(-D+D^2)]\\
i_p(t_2) &= \frac{T_{sw}}{2L_{lk}}[V_{in}(-D+D^2)+nV_{out}(D-2D_\phi-D^2+2DD_\phi)]\\
i_p(t_3) &= \frac{T_{sw}}{2L_{lk}}[V_{in}(2DD_\phi-D+D^2)+nV_{out}(D-D^2)].
\end{aligned} \tag{1}$$

Likewise, the instantaneous currents in case B are calculated as follows:

$$\begin{aligned}
i_p(t_0) &= \frac{-T_{sw}}{2L_{lk}}[(V_{in}(-D+D^2)+nV_{out}(-2DD_\phi+D-D^2)]\\
i_p(t_1) &= \frac{T_{sw}}{2L_{lk}}[V_{in}(-D+D^2)+nV_{out}(2DD_\phi-D-D^2)]\\
i_p(t_2) &= \frac{T_{sw}}{2L_{lk}}[V_{in}(-D+2DD_\phi-D^2)+nV_{out}(-D+D^2)]\\
i_p(t_3) &= \frac{T_{sw}}{2L_{lk}}[V_{in}(-D+2DD_\phi+D^2)+nV_{out}(D-D^2)].
\end{aligned} \tag{2}$$

For the 2-DOF modulation control, the transferred power P can be calculated using the following equation:

$$P(D,D_\phi) = \begin{cases} CD_\phi[2D(1-D)-|D_\phi|], & (D_\phi \le D) \\ CD^2(1-2|D_\phi|), & (D \le D_\phi \le 1-D) \end{cases} \tag{3}$$

where $P > 0$ means that the power is transferred from the input port to the output port and $C = \frac{nV_{in}V_{out}}{2L_{lk}f_{sw}}$.

By contrast, $P < 0$ represents that the power is transferred from the output port to the input port, i.e., the regenerative operation. In addition, the RMS current of the primary-side $I_{p(rms)}$, which can be derived as the function of D and D_ϕ from the current waveform as shown in Fig. 2 [5], is defined as follows: (4) shown at the bottom of the next page where $M = (nV_{out})/V_{in}$ indicates the voltage conversion ratio, $k = V_{in}^2/(12L_{lk}^2 f_{sw}^2)$, $a = (1-M)^2$, and $b = 4M$.

III. 2-DOF Modulation Without ZVS Operation

A. Formulation of Minimum Current Operation

The 2-DOF modulation can be applied to minimize the transformer RMS current, which suppresses the high circulating current in the circuit, i.e., conduction loss reduction of the switches and the transformer. Therefore, the minimum current operation of the DAHB converter in Fig. 2(a) is stated as the optimization problem expressed in the following equation:

$$\begin{aligned} &\text{minimize} && I^2_{p(rms)}(D_{ref},\, D_{\phi,ref}) \\ &\text{subject to} && G_V(D_{ref},\, D_{\phi,ref}) = G_{V,ref}. \end{aligned} \tag{5}$$

It can be used to derive the phase shift reference $D_{\phi,ref}$ and the duty ratio reference D_{ref}.

The virtual conductance G_V is a conceptual variable defined as the ratio of the output current to the input voltage without consideration of power loss, which is derived from the power equation in (3) to simplify the calculation process as follows:

$$\begin{aligned} G_V(D, D_\phi) &= \frac{P(D, D_\phi)}{C} = \frac{2L_{lk}f_{sw}}{nV_{in}}\frac{P(D, D_\phi)}{V_{out}}. \\ &= D_\phi[2D(1-D) - |D_\phi|] \end{aligned} \tag{6}$$

Likewise, the virtual conductance reference $G_{V,ref}$ is defined as a function of the output current reference over the input voltage I_{ref}/V_{in} where the effects of the output voltage V_{out} are removed.

$$G_{V,ref} = \frac{P_{ref}}{C} = \frac{2L_{lk}f_{sw}}{nV_{in}}\frac{P_{ref}}{V_{out}} = \frac{2L_{lk}f_{sw}}{n}\frac{I_{ref}}{V_{in}}. \tag{7}$$

Equation (5) can be solved by the Lagrange multiplier method, where μ is a Lagrange multiplier and a Lagrangian function is defined as

$$\begin{aligned} \mathcal{L}(D_{ref}, D_{\phi,ref}, \mu) &= I^2_{p(\text{rms})}(D_{ref},\, D_{\phi,ref}) \\ &\quad + \mu[G_{V,ref} - G_V(D_{ref}, D_{\phi,ref})]. \end{aligned} \tag{8}$$

In this case, the maximum duty ratio is 0.5 and the phase shift D_ϕ is limited to be within [−0.25 to 0.25] to minimize the RMS current under the same power.

It is formulated as a pair of equations with two unknowns D_{ref} and $D_{\phi,ref}$ as follows:

$$G_{V,ref} = D_{\phi,ref}\left[2D_{ref}(1-D_{ref}) - |D_{\phi,ref}|\right]. \tag{9}$$

$$D_{ref}(1-D_{ref}) = \frac{1}{2\alpha}{D_{\phi,ref}}^2 + |D_{\phi,ref}| \text{ where } \alpha = \frac{a}{3b}. \tag{10}$$

Equation (9) represents the virtual conductance equation derived from the constraint condition in (5). Equation (10) represents the minimum current operation in the steady state, where the current output matches the current reference.

B. Calculation of 2-DOF Modulation References

The solutions are divided into the case of 1-DOF modulation $(D_{\phi,ref})$ and the case of 2-DOF modulation $(D_{\phi,ref},\, D_{ref})$ according to the absolute magnitude of the current reference, $|I_{ref}|$. The modulation scheme can be determined by comparing the virtual conductance reference $G_{V,ref}$ with the conductance criterion $G_{V,cr}$. $G_{V,cr}$ represents the modulation criterion between 1-DOF and 2-DOF controls, where D_{ref} is set to 0.5 for both cases. It can be solved by substituting D_{ref} with 0.5 in (9) and (10) under the condition of $D_{\phi,ref} > 0$ [5]. Consequently, $G_{V,cr}$ is derived as follows:

$$G_{V,cr} = D_{\phi,cr}(0.5 - D_{\phi,cr}). \tag{11}$$

$$D_{\phi,cr} = -\alpha + \sqrt{\alpha^2 + \frac{1}{2}\alpha}. \tag{12}$$

When $|G_{V,ref}|$ exceeds $G_{V,cr}$, D_{ref} is fixed at 0.5 to maximize the transfer power, and $D_{\phi,ref}$ is adjusted to satisfy the constraint in (9), i.e., the region of 1-DOF control. For the 1-DOF control, $D_{\phi,ref}$ can be calculated using the quadratic formula as follows:

$$D_{\phi,ref} = \text{sign}(G_{V,ref})\frac{1 - \sqrt{1 - 16\,|G_{V,ref}|}}{4}. \tag{13}$$

$$D_{ref} = 0.5. \tag{14}$$

When $|G_{V,ref}|$ is less than $G_{V,cr}$, the 2-DOF control can be implemented by solving the simultaneous equations in (9) and (10) as follows:

$${D_{\phi,ref}}^3 + \alpha(D_{\phi,ref}\,|D_{\phi,ref}| - G_{V,ref}) = 0. \tag{15}$$

$${D_{ref}}^2 - D_{ref} + \frac{1}{2\alpha}{D_{\phi,ref}}^2 + |D_{\phi,ref}| = 0. \tag{16}$$

Equation (15) is a cubic equation of $D_{\phi,ref}$ derived by substituting (9) into (10), where D_{ref} is removed. Equation (16) is derived from (10).

The cubic equation, i.e., the third-order polynomial equation, can be solved using either analytical or numerical approaches. The analytical method known as Cardano's formula is applied to solve the cubic equation, which can be digitally implemented in a microcontroller. The desired solution, i.e., the real root of the cubic equation, is obtained using the following equation:

$$\begin{aligned} D_{\phi,ref} &= \text{sign}\,(G_{V,ref}) \cdot (-\frac{1}{3}) \\ &\quad \left[\alpha + \sqrt[3]{\alpha(\beta + \sqrt{\beta^2 - \alpha^4}} + \sqrt[3]{\alpha(\beta - \sqrt{\beta^2 - \alpha^4}}\right] \end{aligned} \tag{17}$$

where $\beta = \alpha^2 - 13.5|G_{V,ref}|$.

$$\begin{aligned} &I^2_{p(\text{rms})}(D, D_\phi) \\ &= \begin{cases} k[aD^2(1-D)^2 + bD_\phi^2(3D(1-D) - |D_\phi|)], & (D_\phi \le D) \\ k[aD^2(1-D)^2 + bD^2(3D_\phi(1-D_\phi) - |D|)], & (D \le D_\phi \le 1-D). \end{cases} \end{aligned} \tag{4}$$

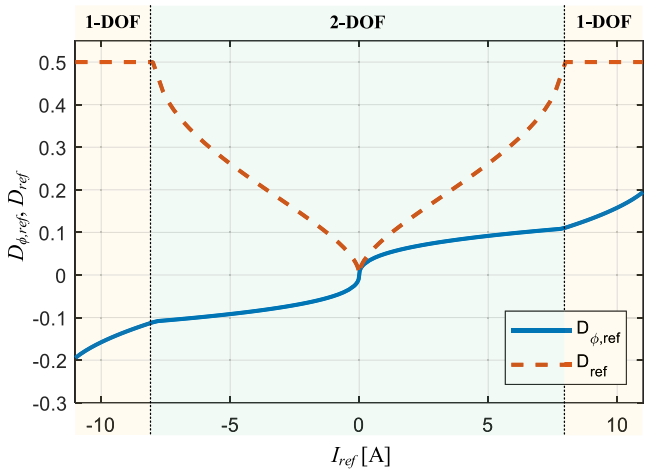

Fig. 3. Trajectories of phase-shift reference and duty ratio reference of 2-DOF modulation without ZVS operation when $M = 0.5$.

TABLE III
SYSTEM PARAMETERS

Parameter	Value
Input voltage, V_{in}	400 V
Output voltage, V_{out}	50 V
Maximum current, I_{max}	11 A
Leakage inductance, L_{lk}	43.2 μH
Switching frequency, f_{sw}	100 kHz
Execution frequency, f_{exec}	50 kHz
Input capacitance, C_{in}	50 μF
Output capacitance, C_{out}	50 μF
Primary-side half-bridge capacitance, C_1, C_2	30 μF
Secondary-side half-bridge capacitance, C_3, C_4	50 μF
Transformer turn ratio, n:1	4:1

After $D_{\phi,ref}$ is derived, D_{ref} can be obtained from the quadratic equation in (15) as follows:

$$D_{ref} = \frac{1-\sqrt{1-4\gamma}}{2} \text{ where } \gamma = \frac{1}{2\alpha} D_{\phi,ref}{}^2 + |D_{\phi,ref}|. \tag{18}$$

Fig. 3 shows the trajectories of $(D_{\phi,ref}, D_{ref})$ according to I_{ref} variations, where the proposed 2-DOF modulation without ZVS operation is implemented. The system parameters are listed in Table III, where M is set to 0.5. For the light-load conditions, $D_{\phi,ref}$ and D_{ref} are changed by 2-DOF control, where $D_{\phi,ref}$ and D_{ref} monotonically increase with the current references I_{ref}. Under the heavy-load conditions, $D_{\phi,ref}$ gradually increases, whereas D_{ref} remains fixed at 0.5 where the 1-DOF control is applied. This shows the monotonic relationship between I_{ref} and $D_{\phi,ref}$ under $I_{ref} < |I_{max}|$, suggesting that 2-DOF control can be feasible as a closed-loop structure. However, the dynamics of $(D_{\phi,ref} / I_{ref})$ and (D_{ref} / I_{ref}) are highly nonlinear and changed depending on the operating condition. Therefore, the conventional PI controller without the LUT method is difficult to increase the dynamics. On the other hand, the model-based control can solve the nonlinear equations to derive optimal solutions in a short time, which improves the dynamic response by applying the calculation part.

TABLE IV
THEORETICAL ZVS TURN-ON CONDITIONS FOR EACH CASE

ZVS condition	S_1	S_2	S_3	S_4
Case A	$i_p(t_0) > 0$	$i_p(t_2) < 0$	$i_p(t_1) < 0$	$i_p(t_3) > 0$
Case B	$i_p(t_0) > 0$	$i_p(t_1) < 0$	$i_p(t_2) < 0$	$i_p(t_3) > 0$

TABLE V
SIMPLIFIED ZVS TURN-ON CONDITIONS FOR EACH CASE

ZVS condition	Case A	Case B
S_1	$2MD_\phi > (M-1)(1-D)$	$2MD_\phi > (M-1)(1-D)$
S_2	$2MD_\phi > (M-1)D$	$2M(1-D_\phi) > (M-1)(1-D)$
S_3	$2D_\phi > (1-M)D$	$2(D_\phi-1) < (M-1)(1-D)$
S_4	$2D_\phi > (M-1)(D-1)$	$2D_\phi > (M-1)(D-1)$

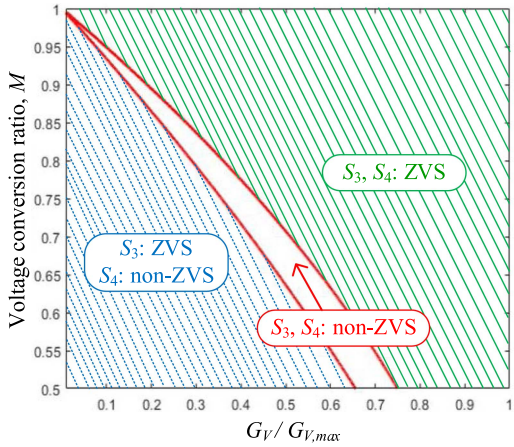

Fig. 4. ZVS turn-ON regions according to G_V and M under the 2-DOF modulation without ZVS operation.

IV. 2-DOF MODULATION WITH ZVS OPERATION

A. Formulation of Minimum Current Operation

The ZVS can be achieved across all switching devices by regulating the circulating current within the high-frequency transformer, which minimizes not only the switching loss but also the electromagnetic interference noise. The ZVS turn-ON conditions of each switch are detailed in Table IV, where the parasitic capacitance of the switches and the magnetizing inductance of the transformer are negligible. The dead time is designed such that there is still a small circulating current to realize the ZVS turn-ON [9]. In this article, the ZVS conditions are focused on the buck mode, i.e., $M < 1$. Furthermore, the boost mode, i.e., $M > 1$, can be analyzed in a similar manner.

The ZVS turn-ON conditions are summarized in Table V based on a time-domain analysis over one switching cycle. Fig. 4 shows the ZVS turn-ON regions depending on the virtual conductance G_V and the voltage conversion ratio M while applying the 2-DOF modulation proposed in Section III. When the DAHB converter is operated in the buck mode, the inequalities in Table V determine the ZVS conditions for all switches. The ZVS conditions of S_1 and S_2 are always satisfied since its right-hand side remains negative under the condition of $M < 1$. Consequently, S_1 and S_2 achieve the ZVS turn-ON regardless of G_V. However, the secondary-side switches S_3 and

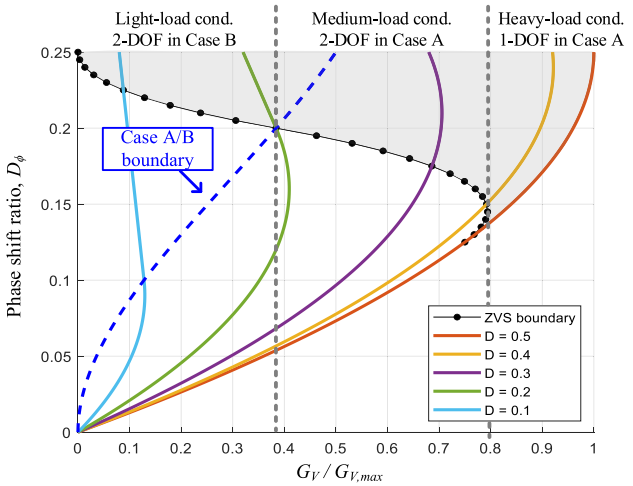

Fig. 5. G_V and fully ZVS turn-ON regions according to D and D_ϕ when $M = 0.5$.

S_4 would fail to achieve ZVS under low G_V, i.e., light-load conditions. The non-ZVS regions increase when M is far away from unity, where the high-side switch S_4 operates in hard switching. Thus, fully ZVS operation for the secondary-side switches cannot be achieved without considering the ZVS conditions.

The minimum current operation while achieving ZVS conditions can be defined as an optimization problem as follows:

$$\begin{aligned} \text{minimize} \quad & I^2_{p(rms)}(D_{ref},\, D_{\phi,ref}) \\ \text{subject to} \quad & G_V(D_{ref},\, D_{\phi,ref}) = G_{V,ref} \\ & z_j(D_{ref},\, D_{\phi,ref}) > 0;\ j = 1,\, 2,\, 3,\, 4. \end{aligned} \tag{19}$$

where z_j denotes the inequalities corresponding to each ZVS condition. The inequality constraints are added to satisfy the ZVS turn-ON of all switches, which minimizes the burden at switching instants.

When the high-side switch S_4 satisfies the ZVS condition, the low-side switch S_3 also ensures the ZVS condition. In other words, the fully ZVS operation is satisfied when S_4 achieves the ZVS constraint [5]. The ZVS criterion can be simplified as a single inequality as follows:

$$2D_{\phi,ref} > (M-1)(D_{ref}-1). \tag{20}$$

Fig. 5 shows the virtual conductance, G_V in (6), and the ZVS criterion in (20) depending on the phase shift D_ϕ and the duty ratio D for the forward operation, i.e., $D_\phi > 0$, where M is set to 0.5. In this case, D_ϕ is limited under 0.25 to minimize the RMS current as aforementioned. The ZVS conditions are satisfied above the ZVS boundary, which are marked as shaded regions. The power flow and RMS current are symmetrical about $D = 0.5$, which means that G_V and the ZVS criterion of D are equal to those of $(1-D)$ for the same D_ϕ. The boundary condition between cases A and B is marked as a dotted line. The 2-DOF modulation with a ZVS operation can be classified into three operating regions: light, medium, and heavy loads. The operating regions should be identified by the discriminants, and the solutions in each region will be derived hereafter.

B. Calculation of 2-DOF Modulation References

For the light-load conditions, the ZVS criterion cannot be satisfied for the operation in case A. Thus, the operation in case B should be guaranteed for the ZVS operation under a certain power level. The boundary condition between cases A and B could be identified by matching D with D_ϕ, i.e., $D = D_\phi$. The duty ratio criterion D_{crL} is easily obtained by substituting D_ϕ with D in (20). Moreover, the conductance criterion $G_{V,crL}$ is derived from (3) as follows:

$$D_{crL} = (-M+1)/(3-M). \tag{21}$$

$$G_{V,crL} = (1-M)^2(M+1)/(3-M)^3. \tag{22}$$

When G_V is lower than $G_{V,crL}$, i.e., $|G_{V,ref}| < G_{V,crL}$, the optimal solution is located on the ZVS boundary, where $I_{p(rms)}$ is minimized while satisfying the inequality in (20). Therefore, the control variable can be formulated using the equations in case B as follows:

$$2D_{\phi,ref} = (M-1)(D_{ref}-1). \tag{23}$$

$$G_{V,ref} = D^2_{ref}[1 - 2\,|D_{\phi,ref}|]. \tag{24}$$

The equations in (23) and (24) are deduced as follows:

$$D_{ref}{}^3 + z_{1,a} D_{ref}{}^2 + z_{1,b} = 0 \tag{25}$$

where $z_{1,a} = \frac{M}{1-M}$ and $z_{1,b} = -\frac{|G_{V,ref}|}{1-M}$.

The cubic equation is solved using Cardano's formula as aforementioned. The 2-DOF modulation references D_{ref} and $D_{\phi,ref}$ can be derived from (25) as follows:

$$D_{ref} = 2\sqrt{-\frac{p_1}{3}}\cos\left(\frac{1}{3}\arccos\left(\frac{3q_1}{2p_1}\sqrt{\frac{-3}{p_1}}\right) - \frac{z_{1,a}}{3}\right), \tag{26}$$

where $p_1 = -\frac{1}{3}(z_{1,a})^2$ and $q_1 = \frac{2}{27}(z_{1,a})^3 + z_{1,b}$.

$$D_{\phi,ref} = \text{sign}(G_{V,ref})\frac{(M-1)(D_{ref}-1)}{2}. \tag{27}$$

For the medium-load conditions, the ZVS criterion is satisfied for the operation in both cases A and B. In this region, the RMS current in case A is smaller than that in case B [5]. Moreover, the ZVS operation can be achieved for the entire range of D_{ref} and $D_{\phi,ref}$ over a certain power level. The maximum value of G_V at the ZVS boundary can be derived using the following optimization problem:

$$\begin{aligned} \text{maximize} \quad & G_V(D_{ref},\, D_{\phi,ref}) \\ \text{subject to} \quad & 2D_{\phi,ref} = (M-1)(D_{ref}-1). \end{aligned} \tag{28}$$

The conductance criterion and the duty ratio criterion at this point are denoted as $G_{V,crH}$ and D_{crH}, respectively. Consequently, $G_{V,crH}$ and D_{crH} are derived as follows:

$$D_{crH} = (3-M)/6. \tag{29}$$

$$G_{V,crH} = (1-M)(M+3)^3/432. \tag{30}$$

When G_V is between $G_{V,crL}$ and $G_{V,crH}$, i.e., $G_{V,crL} < |G_{V,ref}| < G_{V,crH}$, the optimal solution can be obtained by simultaneously solving the ZVS constraint for case A and the

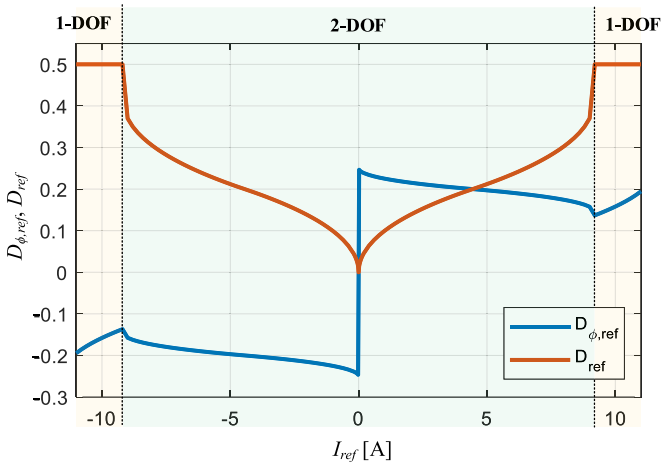

Fig. 6. Trajectories of phase-shift reference and duty ratio reference of 2-DOF modulation with ZVS when $M = 0.5$.

virtual conductance equation as follows:

$$2D_{\phi,ref} = (M-1)(D_{ref}-1). \tag{31}$$

$$G_{V,ref} = D_{\phi,ref}(2D_{ref}(1-D_{ref}) - |D_{\phi,ref}|). \tag{32}$$

The equations in (31) and (32) are deduced as follows:

$$D_{ref}{}^3 + z_{2,a}D_{ref}{}^2 + z_{2,b}D_{ref} + z_{2,c} = 0 \tag{33}$$

where $z_{2,a} = \frac{-9+M}{4}$, $z_{2,b} = \frac{3-M}{2}$, and $z_{2,c} = \frac{M-1}{4} - \frac{|G_{v,ref}|}{1-M}$.

Similarly, D_{ref} and $D_{\phi,ref}$ are derived from (33) as follows:

$$D_{ref} = 2\sqrt{-\frac{p_2}{3}}\cos\left(\frac{1}{3}\arccos\left(\frac{3q_2}{2p_2}\sqrt{\frac{-3}{p_2}} - \frac{4\pi}{3}\right) - \frac{z_{2,a}}{3}\right) \tag{34}$$

where $p_2 = z_{2,b} - \frac{(z_{2,a})^2}{3}$ and $q_2 = \frac{2}{27}(z_{2,a})^3 - \frac{z_{2,a}z_{2,b}}{3} + z_{2,c}$.

$$D_{\phi,ref} = \text{sign}(G_{V,ref})\frac{(M-1)(D_{ref}-1)}{2}. \tag{35}$$

For the heavy-load conditions, the ZVS condition is always satisfied. This means that the optimization problem has an equality constraint only when $|G_{V,ref}|$ is greater than $G_{V,crH}$, i.e., $G_{V,crH} < |G_{V,ref}|$. Therefore, the optimization problem in (19) is entirely consistent with that in (5). In this region, the 1-DOF modulation is applied because $G_{V,crH}$ in (30) exceeds $G_{V,cr}$ in (11). Thus, D_{ref} and $D_{\phi,ref}$ can be derived as follows:

$$D_{ref} = 0.5 \tag{36}$$

$$D_{\phi,ref} = \text{sign}(G_{V,ref})\frac{1-\sqrt{1-16\,|G_{V,ref}|}}{4}. \tag{37}$$

Fig. 6 shows the trajectory of $(D_{\phi,ref}, D_{ref})$ in response to I_{ref} under the 2-DOF modulation with ZVS operation, where the system parameters are listed in Table III. Under the light-load conditions, $|D_{\phi,ref}|$ is greater than D_{ref} to satisfy the ZVS constraints of case B when $|I_{ref}| < 4.4$ A. Under medium-load conditions, $D_{\phi,ref}$ and D_{ref} follows the ZVS boundary of case A. Under heavy-load conditions, D_{ref} is fixed at 0.5, and $D_{\phi,ref}$ gradually increases to maximize the transfer power. The 1-DOF control is applied when $|I_{ref}| > 9.2$ A. The dynamics between the 2-DOF modulation references and the current references are highly nonlinear. Therefore, the voltage controller should be integrated with the 2-DOF modulation schemes to improve the control dynamics.

V. Proposed Unified Voltage Control Scheme

A. Principle of the Proposed Voltage Control Scheme

Fig. 7 shows a block diagram of the proposed unified voltage controller. It consists of the error compensation part to mitigate the effect of parameter errors and the model-based calculation part to enhance the dynamics. The error compensation part adjusts the current reference I_{ref}, to minimize the voltage error incurred by uncertain factors between the model part and the actual system. The model-based calculation part calculates the modulation references, $D_{\phi,ref}$ and D_{ref}, based on the system parameters to quickly track the minimum current operation.

First, the PI controller outputs the feedback current i_{FB} to compensate for the voltage error, where the proportional gain k_{pv} directly responds to the output error, and the integral gain k_{iv} brings the error to zero. Moreover, the feedforward path for the load current I_{load} is incorporated to decouple the effects of the load current disturbance. The feedforward current i_{FF} is modified to suppress the positive feedback effects caused by the load current path, where the load is assumed to have resistive characteristics [19]. However, the positive feedback impacts are reversed in the case of regenerative operations, i.e., a negative load current. Therefore, i_{FF} is multiplied by the voltage ratio between voltage reference and output voltage or vice versa, as follows:

$$i_{FF} = \begin{cases} (V_{out,ref}/V_{out}) \cdot I_{load} & (I_{load} \geq 0) \\ (V_{out}/V_{out.ref}) \cdot I_{load} & (I_{load} \leq 0) \end{cases}. \tag{38}$$

Finally, an output limiter restricts the current reference to the current limit I_{max}. I_{max} can be changed by thermal conditions of the DAHB system, such as the maximum current limit of the half-bridge switches and/or an external temperature. The anti-windup scheme is applied to limit the output voltage reference within the realizable ranges, which can be adjusted using the anti-windup gain k_{av}.

After the current reference I_{ref} is tracked by the voltage controller, the minimum current operation can be achieved through the model-based calculation part. The modulation references trace the desired solution in a short time by directly applying the current reference, the input voltage, and the output voltage owing to the model-based structure. Thus, the proposed voltage controller, unified with the 2-DOF modulation, enhances the control dynamics under the input voltage and load current changes.

Fig. 8 shows a flowchart of the 2-DOF modulation calculation. The ZVS operation could be chosen or not based on the loss distribution of the DAHB converter. Subsequently, the transition between each modulation is decided by the comparisons between $G_{V,ref}$ and the conductance criteria $G_{V,cr}$. It provides the smooth transition between the modulation schemes depending on the load conditions. The modulation references $D_{\phi,ref}$ and D_{ref} are calculated based on the analytic equations. $D_{\phi,ref}$ is

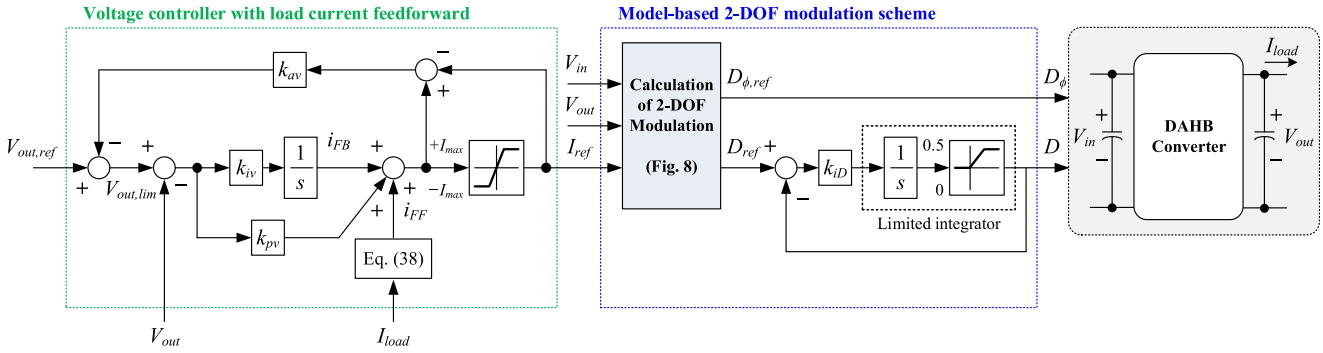

Fig. 7. Block diagram of the proposed unified voltage controller.

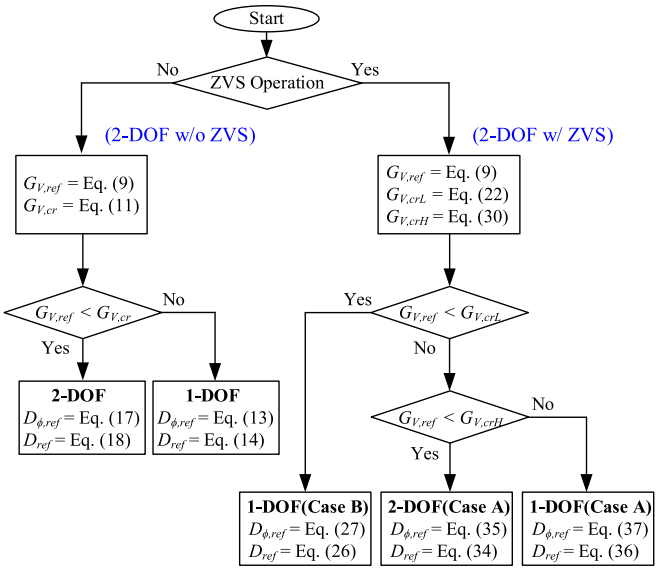

Fig. 8. Flowchart for the 2-DOF modulation calculation.

changed within the range of $[-0.25, 0.25]$ and D_{ref} is within the range of [0, 0.5] to transfer the maximum power in both directions.

In this part, the duty ratio reference D_{ref} determines the voltage ratio between the upper and lower split capacitors. The abrupt changes of D_{ref} would induce *LC* resonance, where the split capacitor voltage oscillates. Therefore, the limited integrator is utilized to slow down and limit the change in D_{ref}. The transfer function of the duty reference controller can be defined as follows:

$$\frac{D(s)}{D_{ref}(s)} = \frac{k_{iD}}{s + k_{iD}} \tag{39}$$

where the dynamics of the duty ratio are determined by the integral gain k_{iD}.

B. Design Procedures of the PI Parameters

In the model-based control schemes, the design principle of the PI controller differs from the traditional concept. The control variables, i.e., the phase shift and the duty ratio, are derived by the model-based calculation part with LCFF rather than by the PI controller. This allows the output voltage to be maintained at the desired value under transient conditions. However, the noise in measurement still affects the stability of the proposed controller. Thus, the phase shift and duty ratio disturbances are considered as design criteria of the PI parameters [19].

There is a tradeoff between dynamics and stability, which is determined by the gains of the PI controller, i.e., k_{pv} and k_{iv}. A high proportional gain can improve the transient response but increases the noise sensitivity. The PI parameters should be designed to maintain dynamic performance while suppressing the effects of measurement noise.

Figs. 3 and 6 show the trajectories of the control variables according to the current reference I_{ref} in the 2-DOF modulations. Assuming that the duty ratio reference (D_{ref}) changes gradually due to the integrator, the phase shift reference ($D_{\phi,ref}$) shows a steep slope in the 1-DOF modulation region, where the measurement noise have a large effect on the phase shift. Defining the rated current as I_{rated}, the variation in the phase shift reference $\Delta D_{\phi,ref}$ can be expressed as follows according to (13):

$$\Delta D_{\phi,ref} \approx \sqrt{\frac{1}{16} - \frac{2L_{lk}f_{sw}I_{rated}}{nV_{in}}} - \sqrt{\frac{1}{16} - \frac{2L_{lk}f_{sw}[I_{rated} + (k_i + k_p)v_{err}]}{nV_{in}}} \tag{40}$$

where v_{err} represents the measurement noise of output voltage. It can be approximated by a Taylor series neglecting higher order terms.

The PI parameters are constrained by the phase shift disturbance $\Delta D_{\phi,dist}$ as follows:

$$(k_p + k_i) \le \frac{nV_{in}\Delta D_{\phi,dist}}{L_{lk}f_{sw}v_{err}}\sqrt{\frac{1}{16} - \frac{2L_{lk}f_{sw}I_{rated}}{nV_{in}}}. \tag{41}$$

The integral gain is designed to be one-tenth of the proportional gain to maintain the phase margin, i.e., $k_{iv} = 0.1k_{pv}$. Thus, the range of PI parameters can be expressed as follows:

$$\begin{aligned} k_p &\le \left|\frac{nV_{in}\Delta D_{\phi,dist}}{L_{lk}f_{sw}v_{err}}\sqrt{\frac{1}{16} - \frac{2L_{lk}f_{sw}I_{rated}}{nV_{in}}}\right| \\ k_i &\le \left|\frac{nV_{in}\Delta D_{\phi,dist}}{10L_{lk}f_{sw}v_{err}}\sqrt{\frac{1}{16} - \frac{2L_{lk}f_{sw}I_{rated}}{nV_{in}}}\right|. \end{aligned} \tag{42}$$

C. Loss Distribution of the Proposed 2-DOF Modulation

The system efficiency and loss distribution can be analyzed in aspects of hardware components and modulation schemes. The comprehensive losses of the DAHB converter are the sum of conduction loss, switching loss of the switching devices, and core loss of the magnetic components such as high-frequency transformers [13], [23].

The conduction losses are calculated by the ON-resistance of switching devices and winding resistances, which are proportional to the square of the RMS current as follows:

$$P_{cond} = I_{p(rms)}^2(R_{ds(on),pri}+R_{mag,pri}+n^2(R_{ds(on),\mathrm{sec}}+R_{mag,\mathrm{sec}})) \tag{43}$$

where $R_{ds(on),pri}$ and $R_{ds(on),sec}$ are the ON-resistances of the primary and secondary side switching devices, whereas $R_{mag,pri}$ and $R_{mag,sec}$ represent the resistance of the magnetic components.

The switching losses consist of turn-ON and turn-OFF losses, where the turn-ON loss occurs only in hard switching. Thus, only the turn-OFF loss is considered under the ZVS turn-ON conditions. The switching loss can be calculated using the switching frequency and the voltages and currents across the switching devices at the switching timing [23].

$$P_{sw(on)} = \frac{1}{2}C_{ds}^2 f_{sw} + \frac{1}{2}V_{dc}I_{ON}t_r f_{sw}$$
$$P_{sw(off)} = \frac{1}{2}V_{dc}I_{off}t_f f_{sw} \tag{44}$$

where C_{ds} denotes the parasitic capacitor, I_{ON} and I_{OFF} indicate the currents at the turn-ON and turn-OFF instants, respectively. t_r and t_f represent the rising time and falling time of the switching devices.

The core losses of the magnetic core depend on the magnetic flux, the switching frequency, the core volume, and the core material, where the Steinmetz equations are widely utilized for the calculation as follows [24], [25]:

$$P_{core} = k \cdot f_{sw}^{\alpha} \cdot (\Delta B_{max})^{\beta} \cdot V_{core} \tag{45}$$

where V_{core} and k are set based on the datasheet values, $\alpha = 1.5$, and $\beta = 2.6$.

Fig. 9 shows the transformer RMS current for different modulation schemes under various voltage conversion ratios and virtual conductance conditions, where the parameters are listed in Table III. Not only the 1-DOF control but also the 2-DOF control without and with the ZVS are presented. The 2-DOF modulation without ZVS achieves the lowest RMS current, regardless of M and P_{out}, which can minimize the conduction loss. By contrast, the 2-DOF modulation with ZVS increases the RMS current on purpose to achieve the ZVS conditions, which would increase the conduction loss. The RMS current of the 1-DOF modulation is smaller than that of the 2-DOF modulation with ZVS, except under the light-load conditions, e.g., $I_{out} < 2$ A for $M = 0.5$.

Fig. 10 shows the loss distributions for different modulation schemes under various load conditions. Loss components are calculated using converter loss analyses [13], where the specifications are listed in Tables III and VI. The 1-DOF control increases not only the switching loss due to the hard switching of the secondary-side switches, S_3 and S_4, but also the conduction loss by the high circulating current under light-load conditions as shown in Fig. 10(a). In contrast, the 2-DOF control without ZVS mode follows the lowest RMS current, which minimizes the conduction loss. Moreover, the switch S_3 could achieve soft switching under light-load conditions, as shown in Fig. 4, resulting in reduced switching loss. The 2-DOF control with ZVS mode decreases the turn-ON loss of secondary-side switches to zero. However, the turn-OFF losses of all switches have increased due to the high circulating current required to achieve the ZVS conditions, resulting in significant switching losses under the medium-load conditions as shown in Fig. 10(b). Under heavy-load conditions, the total losses of each modulation are identical because the 1-DOF modulation is the only option as shown in Fig. 10(c). The advantages of ZVS mode would be evident in high-frequency and high-voltage operations, where

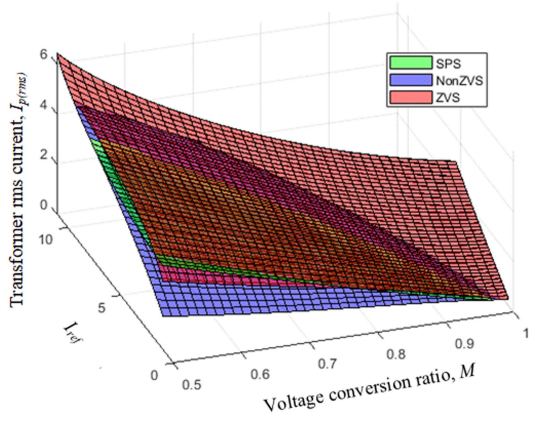

Fig. 9. Surfaces of the transformer RMS current according to G_V and M under different modulation schemes.

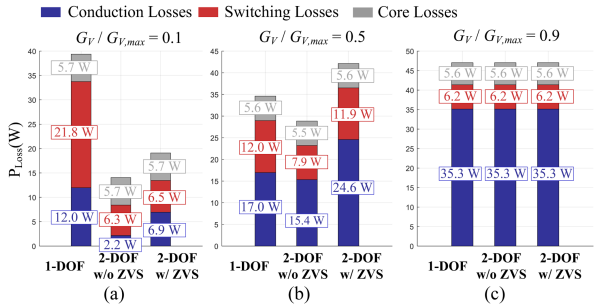

Fig. 10. Loss distributions for different modulation schemes when $M = 0.5$ under (a) light-load conditions, (b) medium-load conditions, and (c) heavy-load conditions.

TABLE VI
HARDWARE COMPONENTS OF THE EXPERIMENTAL PROTOTYPE

Component	Specification	Note
Primary-side switches (S_1, S_2)	650 V, 45 mΩ	C3M0045065D
Secondary-side switches (S_3, S_4)	200 V, 5.3 mΩ	IRF200P222
Winding resistance of transformer	0.6 Ω	PQ4040
Winding resistance of series inductor	0.38 Ω	0077213A7

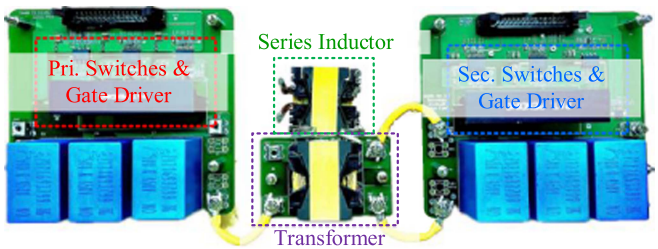

Fig. 11. DAHB converter prototype for experimental verification.

the proportion of the switching loss increases compared to the conduction loss.

VI. Experimental Results

The performance of the proposed voltage controller was verified using the hardware prototype as shown in Fig. 11. The maximum output power is 550 W where the rated input and output voltage are 400 V and 50 V, respectively. The system parameters of the DAHB converter were summarized in Tables III and VI. The output capacitance is significantly low, which clearly shows the dynamic response of the controllers. The leakage inductance L_{lk} is the sum of an external inductance in series with the transformer and an inherent leakage inductance of the transformer. The proposed algorithms were digitally implemented on a DSP, TI TMS320F28377. The gains of the proposed controller k_{pv} and k_{iv} were set to 0.3 and 0.03, respectively, under the condition that $\Delta D_{\phi,dist}$ is 0.01, and v_{err} is 2% of the output voltage.

Fig. 12 shows the output voltage and modulation reference waveforms when the load resistance is changed between 16.7 Ω and 8 Ω, i.e., light- and medium-load conditions. The 2-DOF control without ZVS mode was applied to minimize the RMS current, where $D_{\phi,ref}$ and D_{ref} respond rapidly to the load current changes and reach the steady-state operation in 11 ms, as shown in Fig. 12(a). Furthermore, the 2-DOF control with ZVS mode was implemented, as shown in Fig. 12(b). $D_{\phi,ref}$ and D_{ref} were calculated to trace the ZVS boundary in real time. $D_{\phi,ref}$ was greater than D_{ref} under the light-load conditions to satisfy the ZVS condition. The transition between cases A and B was smoothly achieved in 17 ms because of the unified voltage controller during load changes.

Fig. 13 shows the waveforms under the load variations between 8 Ω and 5.2 Ω, i.e., medium- and heavy-load conditions. In this case, 2-DOF modulation was changed to 1-DOF modulation, where D_{ref} quickly reaches 0.5 under the heavy-load conditions. The model-based calculation part achieved a smooth transition between the modulation schemes. Moreover, the output voltage error was compensated using the voltage controller with LCFF in 21 ms, as shown in Fig. 13(a) and (b).

Fig. 14 shows the experimental waveforms when the input voltage decreases in increments of 40 V from 400 to 320 V, where the load is set to 8 Ω. The input voltage changes take effect immediately to the calculation part, where $D_{\phi,ref}$ and D_{ref} are calculated on the basis of the input voltage. As the voltage conversion ratio M changes, the virtual conductance G_V is adjusted in real time. The output voltage converged to the reference output voltage within 11 ms, respectively, as shown in Fig. 14(a) and (b).

Fig. 15 shows the transient responses when the output voltage reference is changed from 50 to 55 V and vice versa. The load is set to 8 Ω. The proposed voltage controller quickly responds to changes in the output voltage reference owing to the model-based calculation part. The output voltage reference was tracked within 10 ms and 4 ms, respectively, and the output voltage error was minimized using the proposed closed-loop structure. The PI controller minimizes the voltage error induced by the system loss and the dead time of switching devices. The 2-DOF modulation with and without ZVS was integrated with the voltage controller to improve the system efficiency.

Fig. 16 shows the waveforms of the transformer voltages $(v_{ab},\ v_{cd})$, and the inductor current (i_p) for different modulation schemes under 33-Ω load, i.e., $G_V\,/\,G_{V,max} = 0.14$. The 1-DOF control fails to achieve ZVS under the light-load conditions and causes significant circulating current as shown in Fig. 16(a), which increases the conduction and switching losses. The 2-DOF control without ZVS mode minimizes the RMS current by adjusting the phase shift and duty ratio, resulting in hard switching of the secondary-side switches as shown in Fig. 16(b). The 2-DOF control with ZVS mode increases the circulating current to achieve the soft switching of the secondary-side switches as shown in Fig. 16(c). The RMS current of the primary-side $I_{p(rms)}$ is 3.55 A, 1.53 A, and 3.50 A, respectively, according to the modulation schemes. The circulating current is remarkably reduced by applying the 2-DOF control without ZVS mode under the light-load conditions.

Fig. 17 shows the voltage and current waveforms of the transformer under various load conditions when the 2-DOF control with ZVS mode is applied. The asymmetrical duty ratio is utilized to achieve the ZVS conditions while minimizing the RMS current, which results in different voltages between the half-bridge capacitors under the light- and medium-load conditions, as shown in Fig. 17(a) and (b). Otherwise, the symmetric duty ratio is applied under the heavy-load conditions as shown in Fig. 17(c). The inductor current waveforms are presented to verify the ZVS conditions in Table IV at the switching timing, which are marked as a green circle. The ZVS turn-ON of all switches can be achieved not only under heavy-load conditions but also under medium- and light-load conditions by applying the proposed method.

Fig. 18 shows the system efficiency of the hardware prototype under various load conditions for different modulation schemes. The system efficiency is measured by a power analyzer, Yokogawa WT5000, where the loss distributions are difficult to distinguish. Thus, the performance of the modulation schemes is compared in terms of the efficiency from the input port to the output port. Under light-load conditions, the 1-DOF modulation fails to minimize the RMS current and to achieve ZVS, resulting in increased conduction loss due to high circulating currents and increased switching loss due to the hard switching. The ratio of converter losses relative to the transferred power is relatively high under the light-load conditions, reducing the system's efficiency. Compared with the 1-DOF modulation, the 2-DOF modulation with ZVS increases the system efficiency by 15% under light-load conditions. The 2-DOF modulation

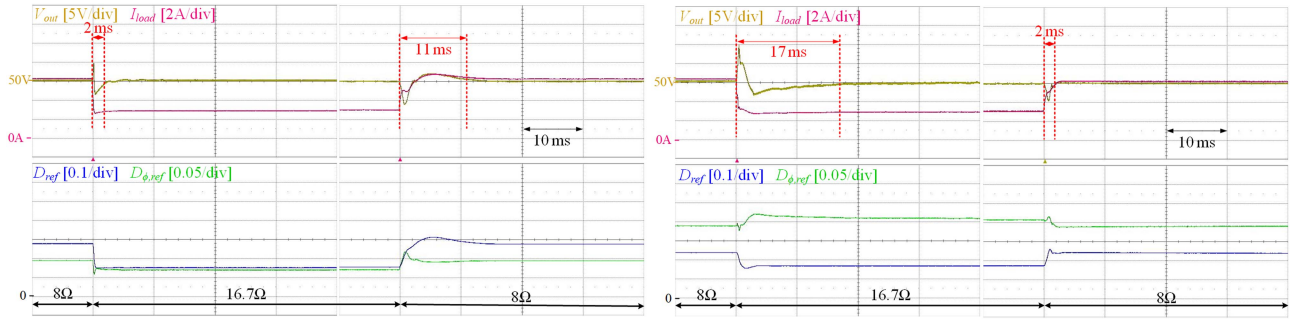

Fig. 12. Experimental results 1: Load resistance variations between 16.7 and 8 Ω of the proposed 2-DOF controller (a) without ZVS mode and (b) with ZVS mode.

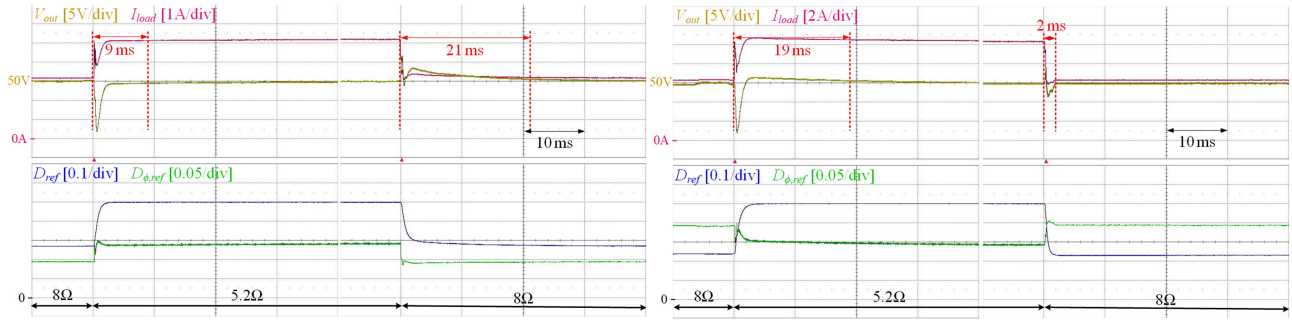

Fig. 13. Experimental results 2: Load resistance variations between 8 and 5.2 Ω of the proposed 2-DOF controller (a) without ZVS mode and (b) with ZVS mode.

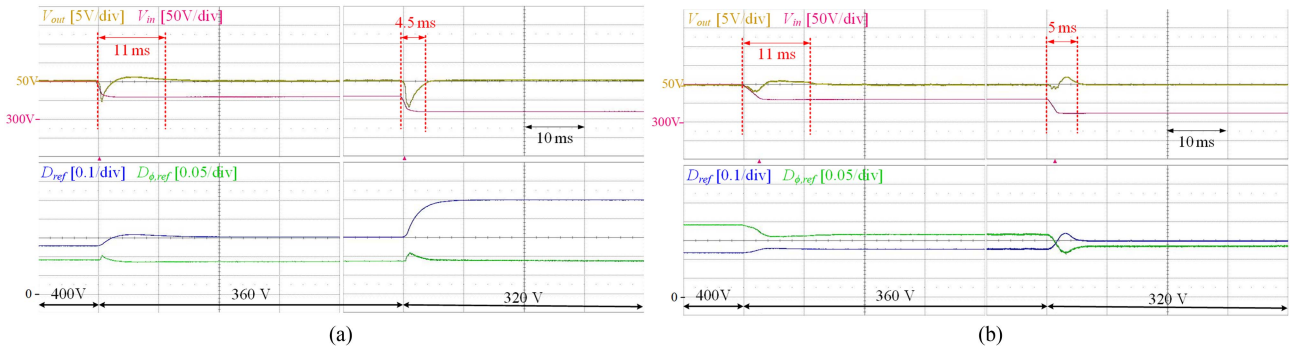

Fig. 14. Experimental results 3: Input voltage variations of the proposed 2-DOF controller (a) without ZVS mode and (b) with ZVS mode.

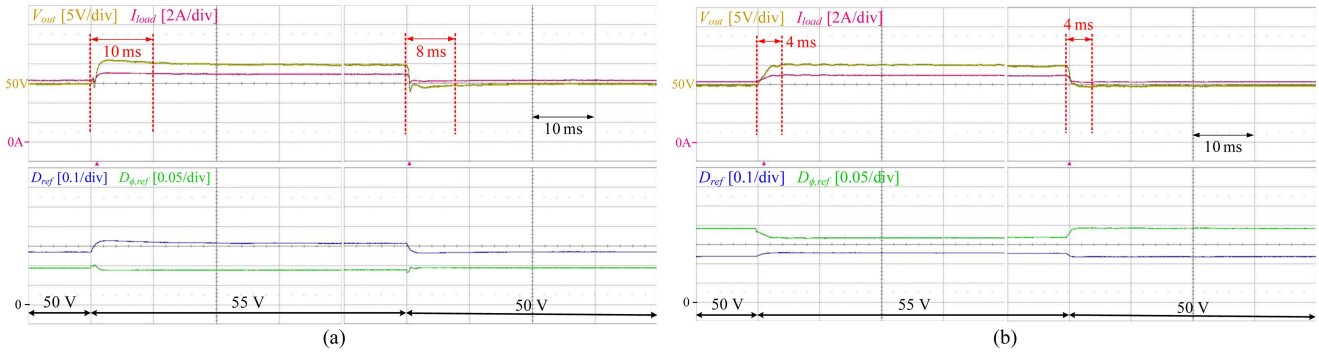

Fig. 15. Experimental results 4: Output voltage reference changes of the proposed 2-DOF controller (a) without ZVS mode and (b) with ZVS mode.

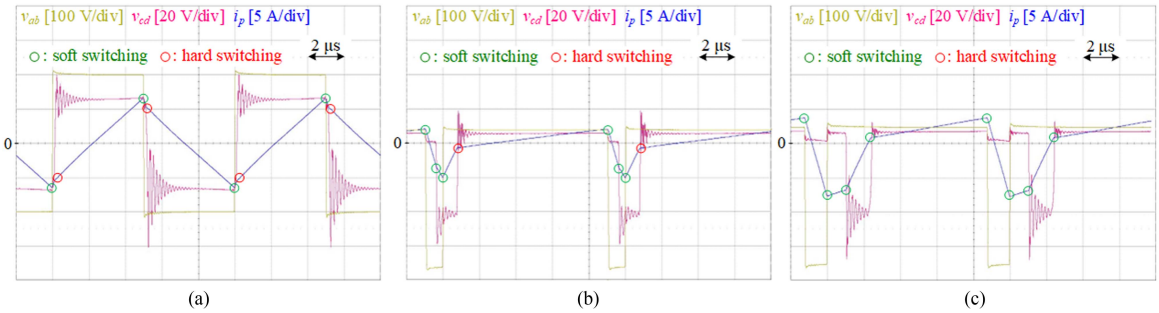

Fig. 16. Experimental results 5: Switching waveforms of the transformer under the light-load condition of (a) 1-DOF controller, (b) 2-DOF controller without ZVS mode, and (c) 2-DOF controller with ZVS mode.

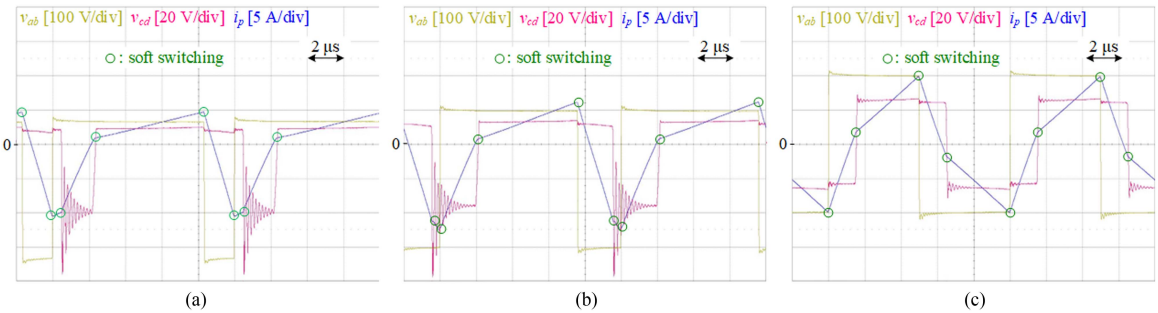

Fig. 17. Experimental results 6: Switching waveforms of the transformer of the proposed 2-DOF controller with ZVS mode under (a) 16.7 Ω, (b) 8 Ω, and (c) 5.2 Ω.

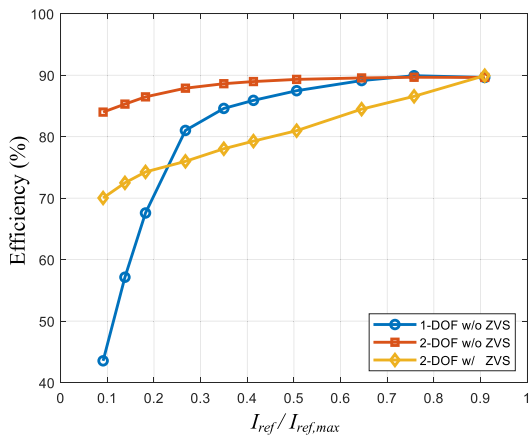

Fig. 18. Overall experimental efficiency under different modulation schemes.

without ZVS further improves efficiency by minimizing the conduction loss, achieving a 30% improvement under light-load conditions. Under the medium-load conditions, the 2-DOF modulation scheme with ZVS operates at the ZVS boundary where a higher circulating current is required. This results in high conduction and switching losses, which leads to the lowest efficiency. Otherwise, the 2-DOF modulation without ZVS achieves high efficiency by minimizing the RMS current. Under heavy-load conditions, the efficiency of each modulation is consistent because the 1-DOF modulation is smoothly achieved by the proposed controller.

Consequently, the 2-DOF modulation without ZVS is highly efficient under all load conditions, where the system efficiency is maintained between 85% and 90% by minimizing the RMS current. In the hardware prototype, the sum of the conduction and core losses is dominant compared to the switching loss as shown in Fig. 10. However, the effect of ZVS operation becomes more significant as the switching frequency increases because the switching loss is greater than the conduction loss. The 2-DOF modulation with ZVS could be more efficient in high-frequency switching applications.

VII. Conclusion

This article analyzed the minimum current operation of the DAHB converter while achieving ZVS conditions or not. Based on these analyses, the 2-DOF modulation schemes for the DAHB converter have been proposed for the bidirectional power flows. The model-based calculation has been inserted to analytically calculate the phase shift and duty ratio references, where the virtual conductance was adopted to optimize the modulation scheme. Moreover, the voltage controller with LCFF has been applied to improve the control dynamics while minimizing the steady-state error. The dynamic response of the proposed method can be improved not only under load changes but also under input voltage and output voltage reference variations. The effectiveness of the proposed method was verified through the experimental results. The proposed method demonstrates excellent dynamic performance even under the 2-DOF modulation both with and without ZVS schemes. The DAHB converter with the proposed scheme can achieve high efficiency and fast dynamics, which is utilized for low-power applications such as auxiliary power or energy systems.

REFERENCES

[1] H. Xie, X. Chen, H. Ouyang, T. Zhang, R. Xie, and Y. Zhang, "An efficient dual-active-bridge converter for wide voltage range by switching operating modes with different transformer equivalent turns ratios," *IEEE Trans. Power Electron.*, vol. 39, no. 8, pp. 9705–9716, Aug. 2024.

[2] N. Hou and Y. W. Li, "Overview and comparison of modulation and control strategies for a nonresonant single-phase dual-active-bridge dc–dc converter," *IEEE Trans. Power Electron.*, vol. 35, no. 3, pp. 3148–3172, Mar. 2020.

[3] S. Shao, H. Chen, X. Wu, J. Zhang, and K. Sheng, "Circulating current and ZVS-on of a dual active bridge dc-dc converter: A review," *IEEE Access*, vol. 7, pp. 50561–50572, 2019.

[4] J. Kim, H.-S. Song, and K. Nam, "Asymmetric duty control of a dual-half-bridge dc/dc converter for single-phase distributed generators," *IEEE Trans. Power Electron.*, vol. 26, no. 3, pp. 973–982, Mar. 2011.

[5] S. Chakraborty and S. Chattopadhyay, "Minimum-RMS-current operation of asymmetric dual active half-bridge converters with and without ZVS," *IEEE Trans. Power Electron.*, vol. 32, no. 7, pp. 5132–5145, Jul. 2017.

[6] S. Chakraborty and S. Chattopadhyay, "Fully ZVS, minimum RMS current operation of the dual-active half-bridge converter using closed-loop three-degree-of-freedom control," *IEEE Trans. Power Electron.*, vol. 33, no. 12, pp. 10188–10199, Dec. 2018.

[7] F. Gao, N. Mugwisi, and D. J. Rogers, "Average modeling of a dual-half-bridge converter modulated with three degrees of freedom," *IEEE Trans. Transp. Electrific.*, vol. 7, no. 3, pp. 1016–1030, Sep. 2021.

[8] M. Kheraluwala, R. Gascoigne, D. Divan, and E. Baumann, "Performance characterization of a high-power dual active bridge dc-to-dc converter," *IEEE Trans. Ind. Appl.*, vol. 28, no. 6, pp. 1294–1301, Nov./Dec. 1992.

[9] F. Xu, J. Liu, and Z. Dong, "Minimum backflow power and ZVS design for dual-active-bridge dc–dc converters," *IEEE Trans. Ind. Electron.*, vol. 70, no. 1, pp. 474–484, Jan. 2023.

[10] D. Mou et al., "Optimal asymmetric duty modulation to minimize inductor peak-to-peak current for dual active bridge dc–dc converter," *IEEE Trans. Power Electron.*, vol. 36, no. 4, pp. 4572–4584, Apr. 2021.

[11] A. K. Jain and R. Ayyanar, "PWM control of dual active bridge: Comprehensive analysis and experimental verification," *IEEE Trans. Power Electron.*, vol. 26, no. 4, pp. 1215–1227, Apr. 2011.

[12] F. Krismer and J. W. Kolar, "Efficiency-optimized high-current dual active bridge converter for automotive applications," *IEEE Trans. Ind. Electron.*, vol. 59, no. 7, pp. 2745–2760, Jul. 2012.

[13] G. G. Oggier, G. O. GarcÍa, and A. R. Oliva, "Switching control strategy to minimize dual active bridge converter losses," *IEEE Trans. Power Electron.*, vol. 24, no. 7, pp. 1826–1838, Jul. 2009.

[14] P. Yang et al., "Optimal dual-side asymmetric modulation strategy for dual active bridge converter to improve efficiency over a wide voltage range," *IEEE J. Emerg. Sel. Topics Power Electron.*, vol. 12, no. 2, pp. 1596–1607, Apr. 2024.

[15] Z. Fan, H. Lu, J. Chai, Y. Li, and X. Sun, "Partition variable frequency and EPS hybrid control to achieve full load range ZVS for dual active bridge converters," *IEEE J. Emerg. Sel. Topics Power Electron.*, vol. 12, no. 1, pp. 143–155, Feb. 2024.

[16] J. Ge, Z. Zhao, L. Yuan, and T. Lu, "Energy feed-forward and direct feed-forward control for solid-state transformer," *IEEE Trans. Power Electron.*, vol. 30, no. 8, pp. 4042–4047, Aug. 2015.

[17] D. Segaran, D. G. Holmes, and B. P. McGrath, "Enhanced load step response for a bidirectional dc–dc converter," *IEEE Trans. Power Electron.*, vol. 28, no. 1, pp. 371–379, Jan. 2013.

[18] W. Song, N. Hou, and M. Wu, "Virtual direct power control scheme of dual active bridge dc–dc converters for fast dynamic response," *IEEE Trans. Power Electron.*, vol. 33, no. 2, pp. 1750–1759, Feb. 2018.

[19] N. Hou, L. Ding, P. Gunawardena, Y. Zhang, and Y. W. Li, "A comprehensive comparison of two fast-dynamic control structures for the DAB dc–dc converter," *IEEE Trans. Power Electron.*, vol. 37, no. 6, pp. 6488–6500, Jun. 2022.

[20] N. Hou, W. Song, Y. Li, Y. Zhu, and Y. Zhu, "A comprehensive optimization control of dual-active-bridge dc–dc converters based on unified-phase-shift and power-balancing scheme," *IEEE Trans. Power Electron.*, vol. 34, no. 1, pp. 826–839, Jan. 2019.

[21] G. -S. Kim, S. -B. Kang, H. -S. Kim, and J. Won, "Model-based dynamic control of two degrees-of-freedom modulation for dual active half-bridge converter," in *Proc. 11th Int. Conf. Power Electron. ECCE Asia*, 2023, pp. 2837–2842.

[22] S. Yin, S. Debnath, R. Wojda, P. Marthi, and M. Saeedifard, "Impact of the transformer magnetizing inductance on the performance of the dual-active bridge converter," in *Proc. IEEE 22nd Workshop Control Model. Power Electron.*, 2021, pp. 1–7.

[23] H. Zhang, X. Tong, J. Yin, and F. Blaabjerg, "Neural network-aided 4-DF global efficiency optimal control for the DAB converter based on the comprehensive loss model," *Energy*, vol. 262, Jan. 2023, Art. no. 125448.

[24] J. Reinert, A. Brockmeyer, and R. W. A. A. De Doncker, "Calculation of losses in ferro- and ferrimagnetic materials based on the modified Steinmetz equation," *IEEE Trans. Ind. Appl.*, vol. 37, no. 4, pp. 1055–1061, Jul./Aug. 2001.

[25] F. Krismer and J. W. Kolar, "Accurate power loss model derivation of a high-current dual active bridge converter for an automotive application," *IEEE Trans. Ind. Electron.*, vol. 57, no. 3, pp. 881–891, Mar. 2010.

Gun-Su Kim (Student Member, IEEE) was born in Seoul, South Korea, in 1999. He received the B.S. degree in electrical engineering in 2023 from Gachon University, Seongnam, South Korea, where he is currently working toward the M.S. degree in next generation smart energy system convergence.

He is currently a Research Engineer with Samsung Electronics, Suwon, South Korea. His research interests include analysis and control of power converters and power electronics systems.

Su-Bin Kang (Student Member, IEEE) was born in Seoul, South Korea, in 2001. She received the B.S degree in electrical engineering in 2023 from Gachon University, Seongnam, South Korea, where she is currently working toward the M.S. degree in next generation smart energy system convergence.

Her research interests include analysis, modeling, and control of power converters.

Hyeon-Sik Kim (Member, IEEE) was born in Busan, South Korea, in 1988. He received the B.S. and Ph.D. degrees in electrical and computer engineering from Seoul National University, Seoul, South Korea, in 2013 and 2019, respectively.

From 2019 to 2021, he was a Principal Research Engineer with Hyundai MOBIS, Seoul, South Korea. Since 2021, he has been with Gachon University, Seongnam, South Korea, where he is currently an Assistant Professor. His research interests include electric machine drives, electric/hybrid vehicles, and power electronic systems in various applications.

Jehyuk Won (Member, IEEE) received the B.S. degree in electronic information systems engineering from Hanyang University, Ansan, South Korea, in 2010, the M.S. degree in electronic and electrical engineering from POSTECH, Pohang, South Korea, in 2012, and the Ph.D. degree in electrical engineering from North Carolina State University, Raleigh, NC, USA, in 2020.

From 2012 to 2015, he was a Researcher with Hyundai Heavy Industries, Yongin, South Korea. From 2020 to 2022, he was a Postdoctoral Research Associate with Oak Ridge National Laboratory, Knoxville, TN, USA. From 2022 to 2024, he was a Research Professor with Gachon University, Seongnam, South Korea. Since 2024, he has been with the Department of Electrical and Electronics Engineering, Kangwon National University, Chuncheon, South Korea, where he is currently an Assistant Professor. His research interests include power converter design and control for solid-state transformers and electric vehicle fast charger applications.